

Achieving the Upper Bound of Piezoelectric Response in Tunable, Wearable 3D Printed Nanocomposites

Desheng Yao, Huachen Cui, Ryan Hensleigh, Parker Smith, Sam Alford, Dominic Bernero, Sydney Bush, Kyle Mann, H. Felix Wu, Marvin Chin-Nieh, Garrett Youmans, and Xiaoyu (Rayne) Zheng*

The trade-off between processability and functional responses presents significant challenges for incorporating piezoelectric materials as potential 3D printable feedstock. Structural compliance and electromechanical coupling sensitivity have been tightly coupled: high piezoelectric responsiveness comes at the cost of low compliance. Here, the formulation and design strategy are presented for a class of a 3D printable, wearable piezoelectric nanocomposite that approaches the upper bound of piezoelectric charge constants while maintaining high compliance. An effective electromechanical interphase model is introduced to elucidate the effects of interfacial functionalization between the highly concentrated perovskite nanoparticulate inclusions (exceeding 74 wt%) and light-sensitive monomer matrix, shedding light on the significant enhancement of piezoelectric coefficients. It is shown that, through theoretical calculation and experimental validations, maximizing the functionalization level approaches the theoretical upper bound of the piezoelectric constant d_{33} at any given loading concentration. Based on these findings, their applicability is demonstrated by designing and 3D printing piezoelectric materials that simultaneously achieve high electromechanical sensitivity and structural functionality, as highly sensitive wearables that detect low pressure air (<50 Pa) coming from different directions, as well as wireless, self-sensing sporting gloves for simultaneous impact absorption and punching force mapping.

1. Introduction

Piezoelectric materials that convert mechanical energy to electrical energy and vice versa, have been widely used in sensing, [1] energy harvesting [2] devices, and microelectromechanical system (MEMS). [3] Among them, lead zirconate titanate (PZT) [4] and

barium titanate (BTO)[5] are the most frequently used piezoelectric ceramic materials for transducer applications. Direct 3D printing of piezoelectric-polymer composites offers a promising solution to fabricating complex piezoelectrics beyond conventional ceramic processing methods which require extensive, time-consuming sintering, may have residual porosity, and have brittle responses. However, due to the functionality-processability tradeoff, the resulting piezoelectric response of the printed nanocomposite is over two ordersof-magnitude lower than pure ceramic.^[6] Increasing particle concentration leads to agglomeration,[7] high viscosity,[8] and significant light absorption, [9] making it difficult to manufacture fully complex microarchitectures or free form-factors. Additionally, the incompatibilities between high stiffness nanoparticle and low stiffness polymer, resulting in poor interfacial adhesion,[10] reduce stress transfer efficiency from the polymer matrix to the piezoelectric inclusions, and suppress the functional performance. Increasing the matrix stiffness was previously shown to be key to enhancing

piezoelectric response,^[11] but it remains unclear if highly-responsive flexible piezoelectric materials are possible.

Recent studies have explored surface functionalization of a low concentration of BTO nanoparticles (below 2 vol%, i.e., 10 wt%) to covalently bind them to the polymer matrix, and have demonstrated appreciable enhancement of the piezoelectric coefficient

D. Yao, H. Cui, P. Smith, S. Alford, D. Bernero, S. Bush, K. Mann, M. Chin-Nieh, G. Youmans, Dr. X. (Rayne) Zheng Department of Mechanical Engineering Virginia Tech Blacksburg, VA 24060, USA E-mail: raynexzheng@vt.edu R. Hensleigh, Dr. X. (Rayne) Zheng Macromolecules Innovation Institute Virginia Tech Blacksburg, VA 24060, USA

The ORCID identification number(s) for the author(s) of this article can be found under https://doi.org/10.1002/adfm.201903866.

Dr. H. F. Wu
Materials Technology R&D
Vehicle Technologies Office
Energy Efficiency and Renewable Energy
U.S. Department of Energy
Forrestal Building, 1000 Independence Avenue, SW
Washington, DC 20585, USA
Dr. X. (Rayne) Zheng
University of California, Los Angeles
420 Westwood Plaza
Los Angeles, CA 90095

DOI: 10.1002/adfm.201903866



www.afm-journal.de

as compared to nonfunctionalized dispersion.^[11,12] This surface functionalization can enhance particle–polymer compatibility, and enables the production of complex, 3D piezoelectric microarchitectures with high concentrations of piezoelectric nanoparticles while maintaining processability.^[1b] However, the mechanism of the electromechanical property enhancement via the interface between the active nanoinclusion and the structural monomer matrix remains elusive. To exploit the potential of multifunctional materials and transducers with designed sensitivity and structural compliance, it is critical to understand the roles of the nanoscale inclusion, the photosensitive monomer and their covalent interface, and probe the upper bound of the multifunctional responses which does not follow a simple rule-of-mixture model.^[13]

In this study, we present the design and additive manufacturing of a class of flexible piezoelectric nanocomposites with high functional responses and a broad tunability of structural properties via tuning the electromechanical properties of the active-structural-interphases. We constructed an effective interphase model to quantify the electromechanical properties of the 3D printable nanocomposites, which takes into account the active nanoinclusion morphology, properties of the structural matrix, as well as the inclusion-matrix interaction of the nanocomposite. Through maximizing the surface functionalization level, we demonstrate through theoretical calculation, numerical, and experimental validations, that the as-fabricated piezoelectric composites approach the theoretical upper bound of piezoelectric coefficients d_{33} at a given piezo-active phase concentration. Breaking the conventional sensitivity/compliance tradeoff, we show that pairs of optimal piezoelectric coefficients and compliance of the as-fabricated piezoelectric composites can be attained, through prudent choices of particle loading parameter, surface functionalization, and UV curable monomer stiffness. Based on these design principles, we demonstrate flexible, robust, and highly sensitive 3D piezoelectric materials as wearables that detect incoming air flow pressures that are otherwise undetectable using commercially available piezoelectric polymers, as well as wireless self-sensing sporting gloves for simultaneous impact absorption and impact force mapping. Our findings provide routes to simultaneously achieve the desired flexibility while retaining high piezoelectric coefficients for 3D printable multifunctional materials for a variety of applications.

2. Result and Discussion

2.1. Measurement of Piezoelectric Responses of 3D Printable Piezoelectric Nanocomposite

The fabrication of piezoelectric nanocomposite material starts with the functionalization of the piezoelectric particles. We use trialkoxysilane-methacrylate functionalized PZT, with reaction conditions optimized to provide maximum grafting^[1b]. After functionalization of the nanoparticles, the functionalization agent is covalently grafted to the piezoelectric nanoparticle surface, **Figure 1a**. The agent provides a sterically hindered surface in the liquid state,^[14] and after curing by UV-light strong covalent chemical bonds (CH₂–CH₂ group), connect the modified piezoelectric particles with the photopolymer matrix. This matrixinclusion linkage enables effective stress transfer between different phases and facilitates composites dispersion uniformity

despite high inclusion content. These modified PZT particles are then high-energy ball milled into an ultraviolet-sensitive monomer with ultrahigh concentrations [1b] (up to 50 vol%, i.e., $\approx\!\!87\text{wt}\%$). This UV-sensitive dispersion is printed with a custom-made large area projection microstereolithography (PµSL) system [1b] where a tape-casting recoating process [15] is designed to ensure accurate control of the colloidal paste thickness prior to UV pattern exposure (Figure 1b; Figure S1a and Section S1, Supporting Information). A variety of as-printed piezo-active materials with complex 3D microarchitectures and flexibilities are shown in Figure 1c–f. To active the piezoelectric polarizations, a 5 V µm $^{-1}$ uniform electric field was applied to pole these piezoelectric nanocomposites for one hour under room temperature [16] (Figure S2 and Section S2, Supporting Information).

To evaluate the surface functionalization and ensure maximum grafting, we measured the response via the Fourier-transform infrared spectroscopy attenuated total reflectance (FTIR-ATR) of thoroughly cleaned PZT particles with various surface agent loadings or functionalization reaction times as shown in Figure 2a,b. The spectrum focuses on the carbonyl and alkene of the methacrylate surface groups nominally at 1710 and 1630 cm⁻¹ respectively. The increasing intensity with higher loading and reaction time indicates increasing grafting of the functionalization agent to the PZT particles until a maximum is reached where no further gain in intensity is achieved. This maximum loading is referred to as "100%." The loading of the surface linker for partially functionalized (50%, 25%) is calculated with respect to this critical concentration. The free methacrylate groups on the fully modified particle surface provide steric interference and favorable interactions with the acrylic prepolymer dispersion allowing high-quality, agglomeration-free state. The piezoelectric voltage output of the as-printed nanocomposite is measured via cyclical loadings from a standard shaker and data acquisition system connected with a 40 M Ω resistor (see Figure S3a,b in the Supporting Information). We fabricated 30 vol% (≈74 wt%) piezo-active material and compared the measured d_{33} constant and voltage output with commercial polyvinylidene fluoride (PVDF) film of identical overall dimension (6 mm \times 6 mm \times 0.5 mm). Both measurements are induced by a shaker (LING DYNAMIC SYSTEMS, LTD. V203) with ≈3 N sawtooth cyclical impact input. Figure 2c shows significantly elevated voltage output via surface functionalization of the piezo-active feedstock, which exceeds that of commercial piezoelectric polymer material, PVDF by over three times. This is attributed to higher piezoelectric charge constant d₃₃ of the 30 vol% (≈74 wt%) functionalized piezoelectric composite ($d_{33} \approx 110 \text{ pC N}^{-1}$) as compared to that of the commercial PVDF ($d_{33} \approx 27$ pC N⁻¹) and previous 3D printed piezoelectric nan ocomposites^[12]($d_{33} \approx 40 \text{pC N}^{-1}$). The piezoelectric charge constant d_{33} , defined as the induced electric charge density per unit applied stress, was evaluated to quantify the piezoelectric behavior of the as-fabricated nanocomposite after calibrating the measurement system with standard piezoelectric films (Section S3 and Figure S3d, Supporting Information).

2.2. Effective INTERPHASE Model of the Functionalized Nanocomposites

Herein, to capture the physical foundation of the observed electromechanical properties at a variety of loading conditions



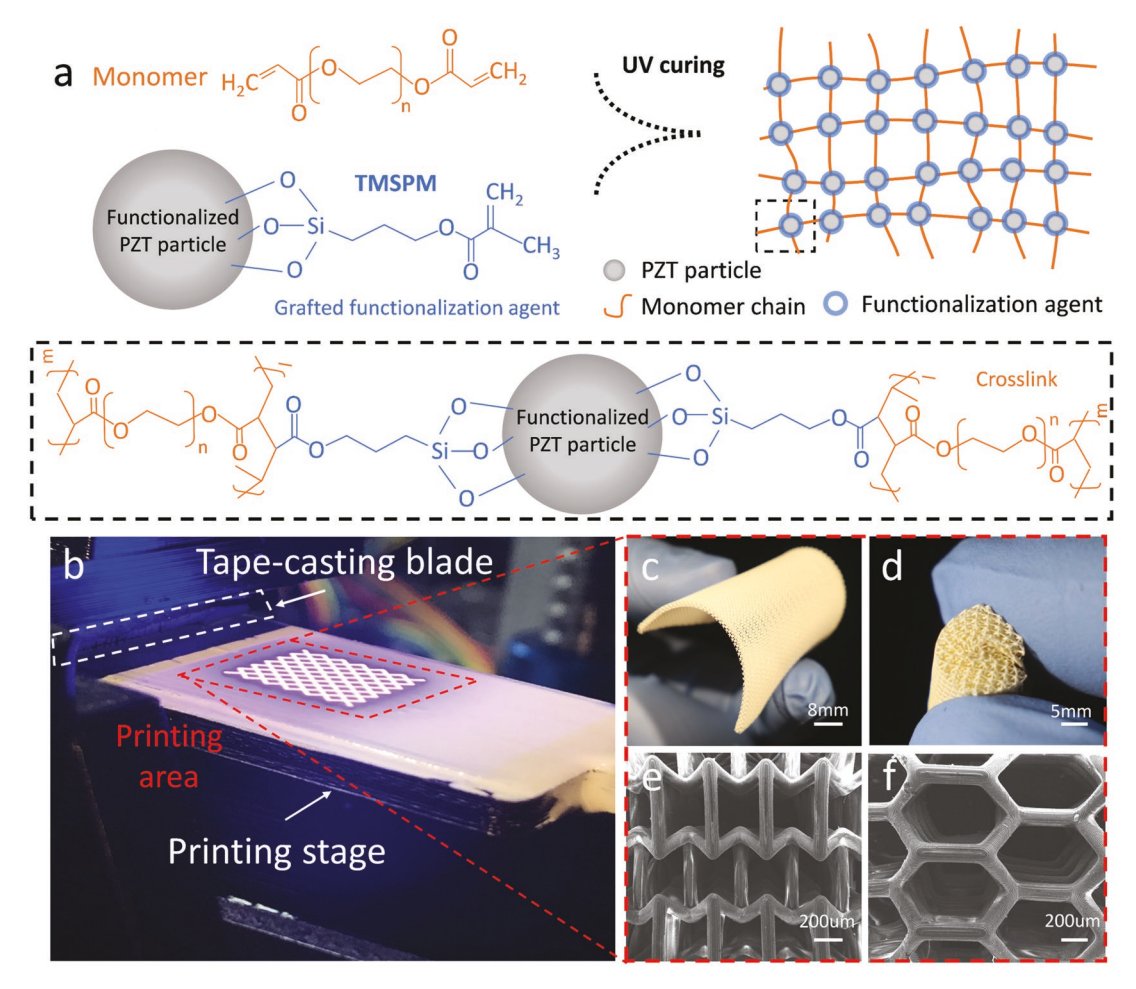


Figure 1. a) Chemical structure of the UV-sensitive monomer matrix and the functionalized PZT particles. b) Custom PuSL fabrication system for piezoelectric nanocomposite. c–f) Additive manufactured piezoelectric complex structures with fine surface finish.

and surface functionalization level, we establish the theoretical model and quantify the effective electromechanical properties that arise from the tunable structural parameters of the active and matrix phases. To predict the functional performance of the nanocomposite, we express the electromechanical properties of the piezoelectric materials as^[17]

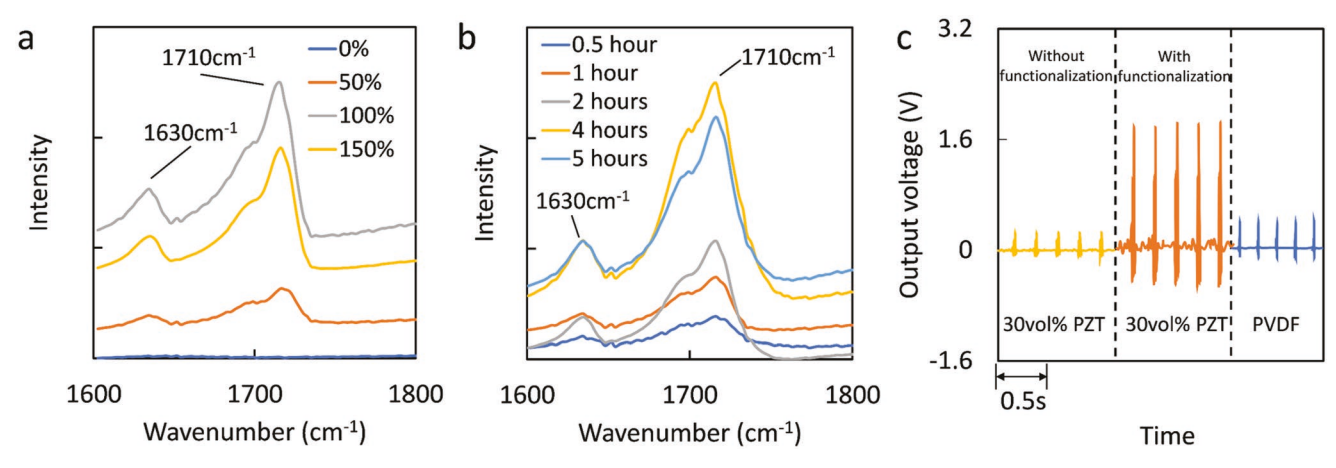


Figure 2. Fourier-transform Infrared Spectroscopy (FTIR) of PZT particles with a) different loading of surface functionalization agent or b) reaction time. c) Comparison of voltage output of functionalized, 30 vol% PZT nanocomposites with nonfunctionalized PZT composite and PVDF polymer (Sigma-Aldrich, MO, USA) induced by the same stress of 48 kPa.

www.afm-iournal.de

$$E_{iJMn} = \begin{cases} C_{iJMn} & \text{for } J, M = 1, 2, 3 \\ e_{nij} & \text{for } J = 1, 2, 3, M = 4 \\ e_{imn} & \text{for } J = 4, M = 1, 2, 3 \\ -\kappa_{in} & \text{for } J = M = 4 \end{cases}$$
 (1)

where C_{ijmn} , e_{imn} , and κ_{in} (i, j, m, n = 1, 2, 3) are the elastic moduli, the piezoelectric constant, and the dielectric constant of the material, respectively. The effective property of the composite is evaluated through the calculation of the electromechanical property matrix E_{ijMn} . The piezoelectric charge constant d_{33} , that quantifies the polarization per unit stress, is calculated as

$$d_{33} = \sum_{i=1}^{3} e_{3ii} C_{ii33}^{-1}$$
 (2)

where C_{ii33}^{-1} represent the corresponding term in the compliance matrix, the inverse of the elastic stiffness matrix C_{ijmn} .

While existing analytical models, including the law-of-mixture model^[13] and laminate models,^[18] etc., have been used to calculate the effective properties of laminates, they are not suitable for characterizing the scenarios where the morphology and the distribution of the active inclusion affect the effective performance of the composite.^[19] Mori–Tanaka model,^[20] a classic micromechanical model, has been used to evaluate the effective property of nanocomposite. However, after surface functionalization, the covalent bonds between the surface linker and the monomer matrix generate an interphase region (**Figure 3**a), which inhibits the relative sliding between the piezo-active inclusion and the polymer matrix.^[21] This enhanced interfacial behavior was not captured in the above-mentioned Mori–Tanaka model which assumes matrix and the inclusion are assumed perfectly bonded.^[22]

Here, to describe the effective electromechanical property of the functionalized piezoelectric nanocomposite, we introduced a generalized effective interphase model to capture the interfacial effect between inclusion and matrix phases. The theoretical prediction of the functional behavior of the nanocomposite takes account of the constituent material electromechanical property (matrix property \mathbf{E}_{I} and inclusion property \mathbf{E}_{II}), nanoinclusion morphology (dilute concentration tensor \mathbf{T}_{II}), and the interfacial interaction between phases (surface functionalization effect) as shown in Figure 3a,b. And the effective property of composite including the interfacial region is given as (detailed derivation in Section S4 in the Supporting Information)

$$\mathbf{E} = \mathbf{E}_{\mathrm{I}} + \left(\left(\nu_{\mathrm{II}} + \nu_{\mathrm{III}} \right) \left(\mathbf{E}_{\mathrm{III}} - \mathbf{E}_{\mathrm{I}} \right) \mathbf{T}_{\mathrm{III}} + \nu_{\mathrm{II}} \left(\mathbf{E}_{\mathrm{II}} - \mathbf{E}_{\mathrm{III}} \right) \mathbf{T}_{\mathrm{II}} \right) \left(\nu_{\mathrm{I}} \mathbf{I} + \left(\nu_{\mathrm{II}} + \nu_{\mathrm{III}} \right) \mathbf{T}_{\mathrm{III}} \right)^{-1}$$
(3)

where **E** is the effective electromechanical stiffness matrix of the as-printed composite which is denoted as E_{iJMn} from Equation (1); **E**_i (i = I, II, III) is the electromechanical property matrix of the matrix phase (I), the active material phase (II) and the interphase region(III), respectively; **I** is the identity matrix; v_i (i = I, II, III) is the volume fraction of the corresponding phase; **T**_{II} and **T**_{III} is the dilute concentration tensor for the nanoparticle and the interphase, which is dependent on the morphology and volume fraction of the particle.

While Poisson's ratio $v^{\rm III}$, piezoelectric constant e and dielectric constant κ of the interface CH_2 - CH_2 groups can be considered consistent with those of the polymer matrix, [23] their Young's modulus CIII are enhanced by the functionalization level at the nanoparticle interface as the surface coverage of the linkers increases. This allows one to tune the effective stiffness \mathbf{E}_{III} of the interphase region by tuning the degree of functionalization. Here, to experimentally identify and evaluate the interphase mechanical properties for our model, nanomechanical characterizations^[24] were conducted on functionalized PZTpolymer films. The normal displacement and the lateral force profiles were extracted from a laterally-scratching indenter (90° conical indenter with radius 738 nm) while holding the constant vertical force that probes into the scratched films (see Section S5 and Figure S4a,b in the Supporting Information). The interphase region is characterized by the area where scratch depth increases or decreases gradually^[25] (see Figure S4a in the Supporting Information). We can then extract the volume fraction v_{III} and the effective modulus C^{III} of the interphase region from the scratch depth profile and the lateral force curve, respectively (detailed derivations see the Experimental Method). Here the superscript I, II, and III in the modulus Ci(i = I, II, II)III) represent the polymer matrix, piezoelectric inclusion, and interphase region, respectively.

We employed the above-mentioned effective interphase scheme and calculated the piezoelectric charge constant d_{33} of the as-fabricated composite with the interphase parameters (volume fraction $\nu_{\rm III}$ and effective electromechanical stiffness E_i) for both the functionalized and nonfunctionalized case, respectively (Figure 3b). As shown in Figure 3c, we plot the d_{33} constants against a range of particle concentrations to see the effect of surface functionalization between the PZT nanoparticle and monomer. Additionally, using the model we quantify the effect of UV curable matrix stiffness, the morphology of nanosized inclusion, and the inclusion-matrix interfacial interaction by configuring the effective stiffness matrix $E_{\rm I}$, Eshelby matrix S and effective modulus of the interphase region $C^{\rm III}$ in the generalized effective interphase model herein, as will be described in the later section.

To validate our theoretical prediction on the surface functionalization effect, we conducted numerical analysis in the COMSOL Multiphysics finite element analysis (FEA) software. [26] The material properties of the piezo-active inclusion, the interphase region, and the monomer matrix are consistent with those used in the theoretical model (detailed material property in Tables 1 and 2). We establish a cubic representative volume element (RVE)[27] model to simulate the effective piezoelectric response of the functionalized nanoparticle matrix over a wide range of the particle loading and inclusion aspect ratios. The periodic boundary conditions (PBC)[27] are enforced to ensure the RVE effectively characterizes the deformation of the macroscopic piezoelectric nanocomposite. In addition, to prevent the rigid body motions and to provide a zero-potential surface for voltage output, the bottom surface of the RVE is fixed in 3-direction and grounded. The piezoelectric voltage output of the RVE is induced by the input stress applied at the top surface (Figure 3d), where the color represents the magnitude of the induced voltage. An elevated voltage output trend can be readily visualized with increasing www.advancedsciencenews.com www.afm-journal.de

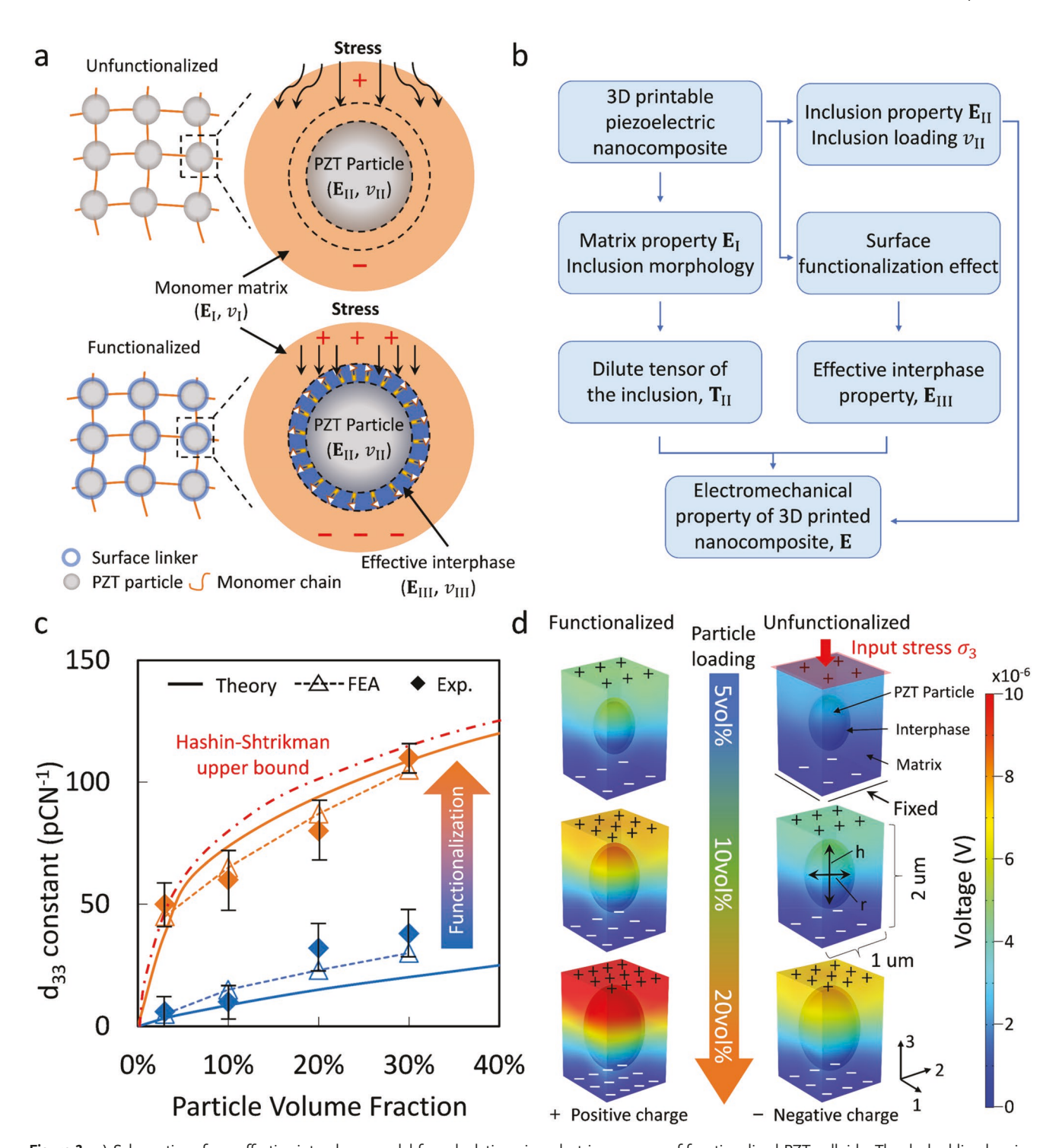


Figure 3. a) Schematics of our effective interphase model for calculating piezoelectric response of functionalized PZT colloids. The dashed lined region represents the effective interphase with electromechanical properties (E_{III}, ν_{III}) formed by the covalent linkage from surface functionalization that connects the active and monomer phase. For nonfunctionalized case the property of such effective interphase approaches zero and can be incorporated into the model. b) Flow chart summarizing the effective interphase model for calculating the electromechanical performance of the 3D printable piezoelectric nanocomposite. c) Theoretical numerical and experimental results of piezoelectric charge constant d_{33} of functionalized and unfunctionalized nanocomposite against a range of particle volume loadings. d) FEA results of functionalized (Left) and nonfunctionalized (Right) RVE with different volume fractions.

volume fractions in functionalized and unfunctionalized cases, all induced by the same external stress. The piezo-electric charge constant d_{33} of the RVE is evaluated by the

ratio between the effective electric displacement $D_3^{\rm eff}$ (average of the electric displacement on the top surface) and the input mechanical stress $\sigma_3^{\rm input}$ as

www.advancedsciencenews.com www.afm-iournal.de

Table 1. The material property of PZT-5H particle.

| Relative dielectric constant | Dielectric dissipation factor | $k_{\rm p}$ | k ₃₃ | k ₃₁ | k ₁₅ | d_{33} (10 ⁻¹² CN ⁻¹ or 10 ⁻¹² mV ⁻¹) |
|------------------------------|-------------------------------|--|--|--|--|--|
| 1900 | <2.00 | 0.63 | 0.72 | 0.36 | 0.68 | 400 |
| d ₃₁ | d ₁₅ | g_{33} (10^{-3} VmN $^{-1}$ or 10^{-3} m 2 C $^{-1}$) | $-g_{31}(10^{-3} \text{ VmN}^{-1} \text{ or } 10^{-3} \text{ m}^2\text{C}^{-1})$ | g_{15} (10^{-3} VmN $^{-1}$ or 10^{-3} m 2 C $^{-1}$) | Young's Modulus (10 ¹⁰ Nm ⁻²) C ^{II} 11 | C^{II}_{33} |
| 175 | 590 | 24.8 | 12.4 | 36 | 6.3 | 5.4 |

$$d_{33} = \frac{D^{\text{eff}}}{\sigma_{33}} \tag{4}$$

Moreover, we measured the piezoelectric coefficients of the 3D printed piezoelectric materials with preconfigured parameters (with and without functionalization, particle volume loading v_{II} and matrix modulus C^{I}). The as-fabricated piezoelectric nanocomposites were polarized (see Section S2 in the Supporting Information) and then assembled to remove the triboelectric effect (see Figure S3a in the Supporting Information). The stress induced voltage output was quantified through a measuring circuit as shown in Figure S3c (Supporting Information), and the piezoelectric charge constant was calculated with this voltage (see Section S3 in the Supporting Information). We observed over ten times enhancement of piezoelectric charge constant (d_{33}) through surface functionalization at 3 vol% (≈17 wt%) PZT particle loading (Figure 3c), consistent with theoretical predictions and numerical simulations. Piezoelectric charge constant was increased over 100% at higher PZT volume fraction (for example from 38 to 110 pC N^{-1} at 30 vol%, i.e., \approx 74 wt% concentration). This consistency between theoretical prediction, numerical analysis, and experimental measurement, as shown in Figure 3b, indicates that generalized effective interphase model could precisely evaluate the functional performance of nanocomposite.

Here, we invoked the Hashin–Shtrikman as the theoretical upper bound of the piezoelectric property of nanocomposite as^[28] (detailed derivations see Section S6 in the Supporting Information)

$$\mathbf{P}_{\text{upper}} = \mathbf{P}_{\text{II}} + (1 - \nu_{\text{II}}) \left\{ (\mathbf{P}_{\text{I}} - \mathbf{P}_{\text{II}})^{-1} + \nu_{\text{II}} \mathbf{S} \mathbf{P}_{\text{I}}^{-1} \right\}^{-1}$$
(5)

where $P_i(i=I, II)$ is the effective compliance matrix of the monomer matrix (i=I) and the piezo-active inclusion (i=II), respectively (detained definition in Section S6 in the Supporting Information); ν_{II} is the particle volume fraction of the nanocomposite; **S** is the piezoelectric Eshelby matrix. As indicated in the Figure 3b, the electromechanical property of the composite significantly is enhanced via particle surface functionalization, approaching the theoretical upper bound.

Table 2. The material property of the monomer matrix ($M_n = 700$) and the interphase.

| | Relative dielectric constant | Young's Modulus C^i ($i = I,III$) (10^6 Nm^{-2}) | Poisson's Ratio v^i ($i = I,III$) |
|----------------------------------|------------------------------|---|---------------------------------------|
| Monomer matrix | 7 | 450 | 0.4 |
| Interphase (functionalized) | 7 | 1380 | 0.4 |
| Interphase (unfunctionalized) | 7 | 178 | 0.4 |

2.3. Multifunctional Design Map of Functionalized Piezoelectric Nanocomposite

The effective interphase framework presented here allows us to access the effects of constituent parameters from the 3D printable raw material feedstock on the electromechanical properties of the bulk nanocomposites. Our methodology enables users to reverse design 3D printable feedstock parameters that can achieve target electromechanical and structural properties after printing. To optimize the piezoelectric performance, we investigated the piezoelectric property of the composites with a range of polymer matrix moduli, morphologies of the perovskite inclusion, and the interfacial strength between the active and inactive phases via controlling functionalization. Increasing the molecular weight (M_n) of the uncured monomer feedstock decreases polymer crosslink density during the UV curing process, and lowers the mechanical modulus, Figure 4a. This allows us to modulate the electromechanical property E_I of the matrix phase, by tuning the molecular weight/mechanical modulus of the polymer C^{I} . Additionally, we employed our model to tune the functional performance of the piezoelectric nanocomposite via varying the morphology of the piezo-active nanomaterials. An enhanced piezoelectric charge constant d_{33} is achieved via increasing the aspect ratio (h/r) of the active phase while maintaining particle concentration, Figure 4b. Increasing the grafting density elevated the resulting effective electromechanical properties of the interphase (EIII) based on our effective interphase model, resulting in elevated piezoelectric constants (d_{33}) at a given nanoinclusion loading (Figure 4c).

By tuning the aspect ratio of functionalized nanoparticle inclusion and the polymer matrix stiffness of the piezo-electric nanocomposite, a wide range of composite stiffness along with high functional response can be simultaneously attained. As shown in Figure 4d, we present the design map for obtaining multifunctional property pairs (piezoelectric charge constants and structural compliance) via configuring the monomer modulus and parameters of the functionalized PZT nanoparticle inclusions. The piezoelectric charge con-

stant d_{33} of the printable nanocomposite is plotted against a range of volume loading of the PZT particles and the UV curable monomer stiffness. A series of surfaces are generated where each point on the surface corresponds to a set of design parameters (i.e., particle volume fraction $v_{\rm II}$, monomer matrix stiffness $C^{\rm I}$, and the aspect ratio of the piezo-active inclusion h/r). The height of the surfaces represents the magnitude of d_{33} , and the color indicates the effective

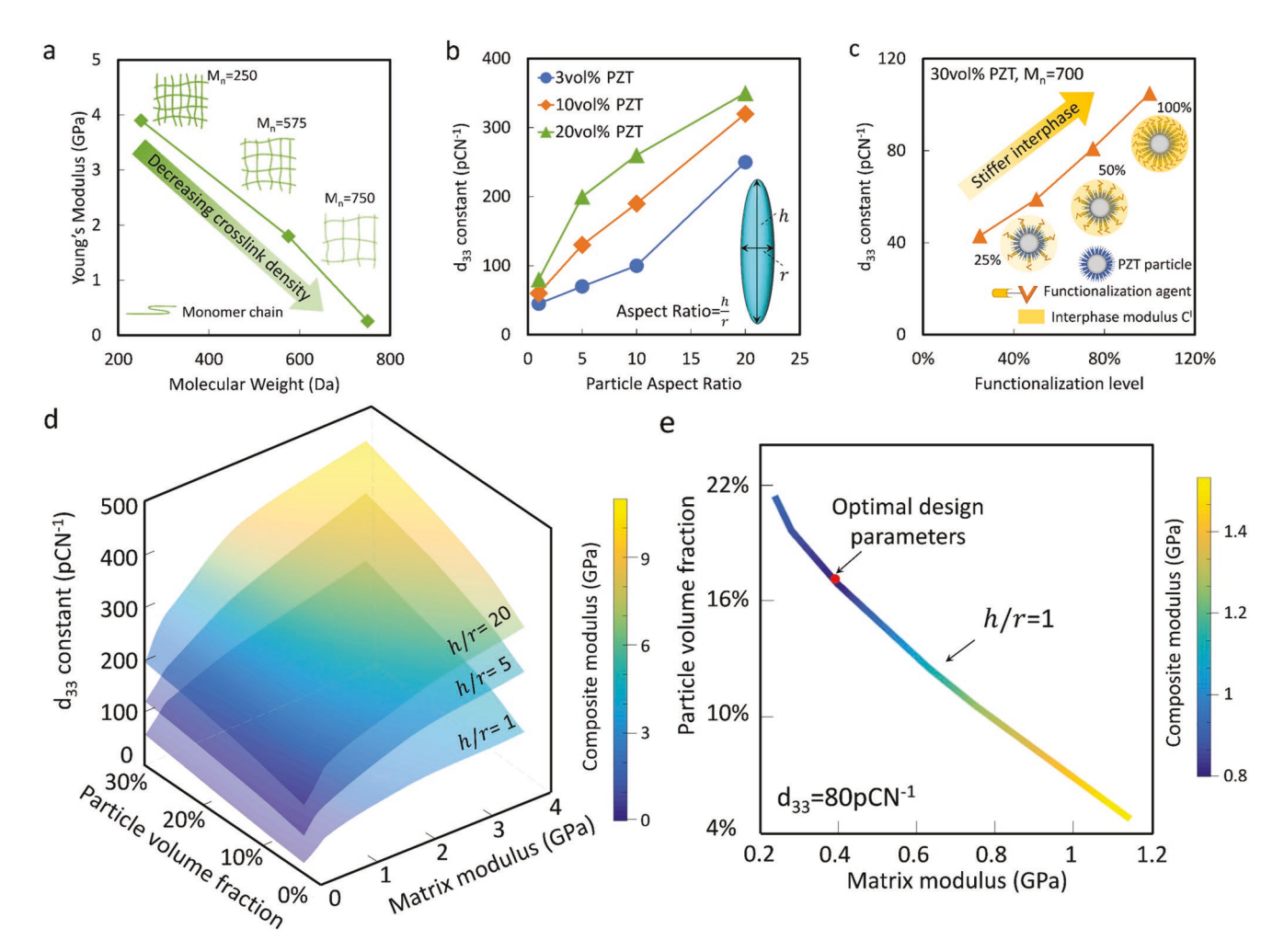


Figure 4. a) The measured Young's modulus of the UV cured monomer matrix with different molecular weight. b) The effect of functionalized inclusion aspect ratio at a constant volume fraction predicted by the theoretical model. d_{33} increases with the aspect ratio of PZT particle. c) The theoretically predicted piezoelectric charge constant of the 30 vol% PZT composite with a range of functionalization level (matrix molecular weight, $M_n = 700$). d) Design map (d_{33} , E) of the 3D printable multifunctional piezoelectric nanocomposites as a function of nanoparticle loading within the dispersion and monomer stiffness. Each surface represents functionalized nanocomposite with a constant aspect ratio of the nanoparticle. e) The optimal combination of the design parameters with given piezoelectric charge constant.

mechanical modulus of the nanocomposite. For instance, with a target piezoelectric charge constant (i.e., $d_{33}=80~{\rm pC~N^{-1}}$), the mechanical stiffness of the resulting composite is modulated via tuning the stiffness of the monomer and the PZT particle loading (Figure 4d) volume fractions. Within the design curve, where the color for each point represents the Young's modulus of the resulting composite (from softer to stiffer), a combination of volume fraction of the PZT inclusion and the monomer stiffness can be configured to reach the target d_{33} constant.

The requirement of high stiffness for high-response makes achieving highly flexible piezoelectric sensors particularly challenging. Wearables and biomedical implants may particularly require low-stiffness piezoelectric sensors due to the strains and soft tissues involved, but simultaneously require high-response due to their low sensor input forces. Our modeling may direct nanocomposite development towards this area of highly-flexible and high-response nanocomposites (see Section S7 and Figure S5 in the Supporting Information). We compared

the designed performance of the piezoelectric nanocomposite with that of existing 3D printed piezoelectrics [6a,11,12,29]. As shown in **Figure 5**, the designed nanocomposite exceeds the functional property of other 3D printable piezoelectrics, while occupying a wide range of compliance range (i.e., from 5.5×10^{-11} to $3 \times 10^{-8} \text{Pa}^{-1}$). Our design strategies imply that target structural flexibility while retaining high sensitivity and detection ranges can be simultaneously achieved via rational selections of constituent material parameters, as will be demonstrated below.

2.4. Flexible, Conformal Self-Sensing Material for Low Air Pressure Detection

The possibility of achieving high sensitivity and flexibility of the bulk piezoelectric composites motivated us to explore its potential applications as conformal highly sensitive air flow sensor, where the pressure induced by air flow www.advancedsciencenews.com www.afm-journal.de

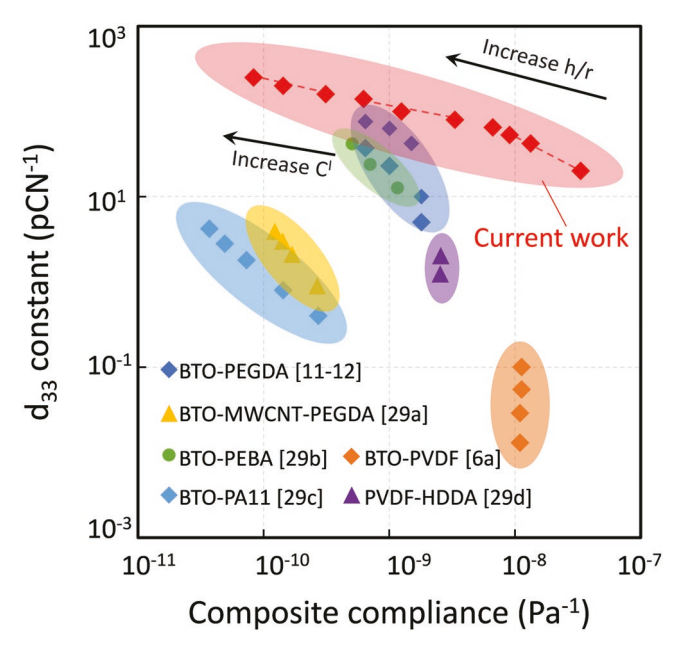


Figure 5. Comparison of piezoelectric charge constant d_{33} and mechanical compliance between piezoelectric nanocomposite presented in this work with other 3D printed composite materials.

(lower than 50 Pa) could be detected. Here, we fabricated a 15 mm \times 15 mm \times 3 mm (one layer of 5 \times 5 unit cells) microarchitected octet-truss lattice structure ($d_{33} \approx 38 \text{ pC N}^{-1}$) with the 3 vol% (≈17 wt%) piezo-active colloidal and attached it on a curved surface, as shown in Figure 6a-c. The radius and the node-to-node length of each strut are 150 µm and 1.8 mm, respectively. We used a UV light source with 14.8 mW cm⁻² light power intensity to solidify each layer of the piezoelectric colloidal. Stretchable, paintable silver electrodes (TED PELLA, Leitsilber 200 Silver Paint) are painted on both sides of the lattice and connected to two copper leads. The voltage outputs of the conformal piezoelectric lattice induced by air flow were collected with a data acquisition system (NI USB-6356). The air flow with different flow direction (Θ) was applied via squeezing a 3 mL pipet with a constant distance between the sensor and pipet. The air pressure was calibrated using a highly sensitive precision force gauge (DBCR-20N APPLIED MEASURE-MENTS LIMITED) prior to the experiment. The highest voltage (≈3 mV) is observed at inflow angle 90°, while the signals are reduced (\approx 2 mV) with other two angles ($\Theta = 45^{\circ}$ and 135°), as shown in Figure 6d. Additionally, we compared the piezoelectric voltage output of a PVDF film and a nonfunctionalized lattice with the functionalized piezoelectric lattice. As shown in Figure 6e, the functionalized piezoelectric flexible sensor

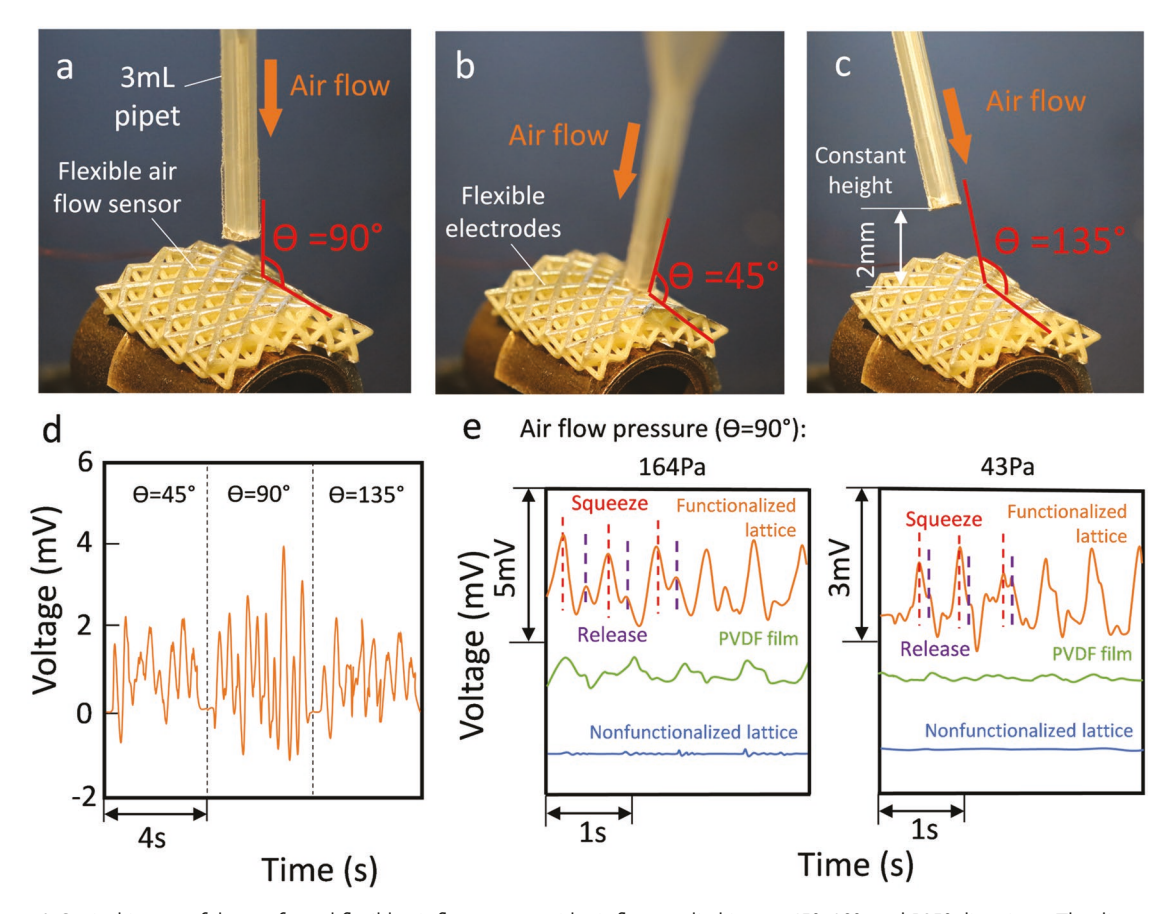


Figure 6. a–c) Optical image of the conformal flexible air flow sensor with air flow applied in $\Theta=45^\circ$, 90°, and 135° directions. The distance between the pipet and the lattice was kept as 2 mm. d) Voltage output of the flexible air flow sensor as a function of time with air flow applied in $\Theta=45^\circ$, 90°, and 135° direction. e) Voltage output of the functionalized lattice, PVDF film and the nonfunctionalized lattice as a function of time. The air flow is generated by squeezing or releasing the pipet continuously. Θ was kept as 90°.

ADVANCED FUNCTIONAL MATERIALS

generates \approx 3 and \approx 1 mV voltages with 164 and 43 Pa air pressure, respectively, while the PVDF can only detect high air flow pressure (164 Pa) with \approx 0.8 mV output and not detectable at 43 Pa. The nonfunctionalized lattice failed to detect air low. The high sensitivity at ultralow-stiffness highlights their potentials as highly sensitive yet flexible and conformal wearables not achievable in current transducer materials.

2.5. Wireless, Self-Sensing Boxing Glove

In addition to the low-pressure detection, we demonstrated the case where mechanical stiffness, energy absorbing, and high

magnitude pressure sensing mapping capabilities were introduced into a sporting wearable device. Here, we 3D printed flexible piezoelectric lattice with stretch dominated microarchitectures with a designed thickness (5 mm) and then inserted into a boxing glove (Figure 7a) to provide spatially resolved and time-resolved mapping of reaction punching forces exerted to knuckles of the hand during boxing activities. The overall dimension of the lattice is $50~\text{mm} \times 80~\text{mm} \times 5~\text{mm}$, while each impact probing area is $10~\text{mm} \times 10~\text{mm}$. The radius and the node-to-node length of the strut are $300~\text{\mu m}$ and 3~mm, respectively. After polarization, the entire 3D printed piezoelectric lattice is active and can be probed from anywhere within the material, providing the new opportunity for sensing where

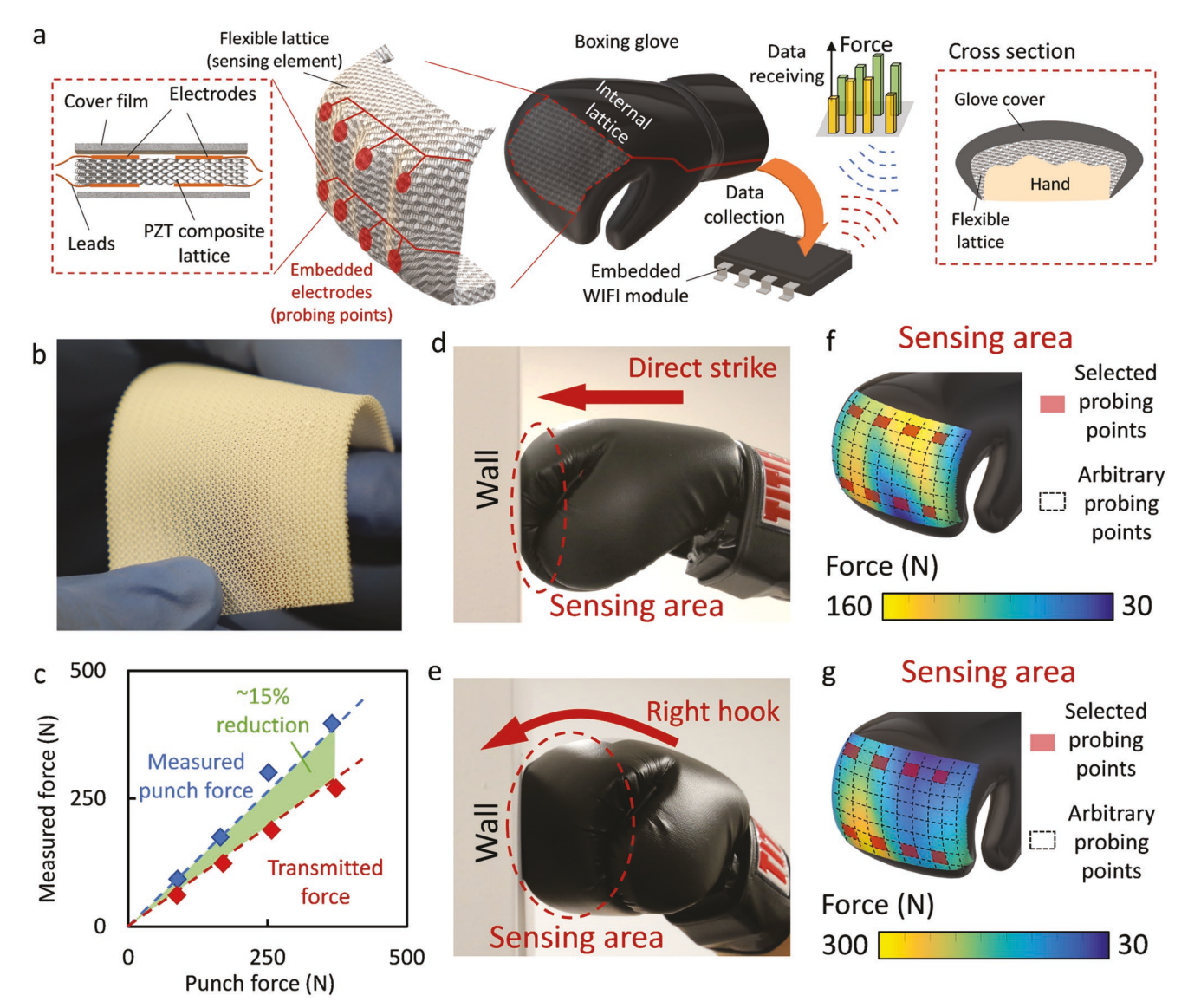


Figure 7. a) Schematics of the wireless self-sensing boxing glove. A 3D printed flexible piezoelectric lattice with stretch dominated microarchitectures is inserted into a boxing glove to provide spatially resolved and time resolved mapping of reaction punching forces exerted to knuckles of the hand during boxing activities. b) Optical image of the flexible, self-sensing lattice. c) Measured punch force and transmitted force versus the applied punch force. The green shaded area between the measured punch force and transmitted force reveals energy absorption of the flexible lattice. d,e) Optical image of the glove when it hits a wall by direct strike and right hook, respectively. f,g) Spatial distribution of force magnitudes obtained from the prescribed electrodes attached on the lattice. The red shaded area denotes the probing points while the dashed lines denotes other locations where the electrodes can be attached to read data output.



www.afm-iournal.de

user configures and defines arbitrary locations for sensing and data output where electrodes are applied. The lattice overall dimension, modulus, and piezoelectric charge constant $(d_{33} \approx 42 \text{ pC N}^{-1})$ are calibrated using force sensor to ensure that the highest punching force that an athlete could produce are within the linear elastic detection range of the lattice material within the boxing glove (Section S8 and Figure S6a, Supporting Information). Here, eight pairs of electrodes corresponding to the knuckles of a hand are attached onto the 3D printed lattice. We integrate our self-sensing, energy absorbing composite with a microcontroller (WEMOS D1 Mini) and multiplexer (BOB-09056, SparkFun Electronics), which allow the data from the eight pairs of electrodes to be sent, received, and hosted over a Wi-Fi connection. As shown in Figure 7a (cross section), we then attach the lattices conformal to the hand and embedded it into a sport boxing glove (Title Classic Boxing Gloves). The stress-induced voltages from the lattice are then wirelessly transmitted to a data receiving devices (cell phone) with a custom-made user interface to read the force data. With the calibrated d_{33} constants and force measurements of the lattices, force magnitude distributions are displayed onto the custom user interface. Figure 7b shows the as-fabricated conformal lattice. Figure 7c plots the measured punch force magnitude of a series of applied, calibrated forces (from 50 to 400 N) on the as-fabricated conformal lattice. The significant gap (green area) between the punch force and transmitted force reveals the structural impact absorbing capabilities of the smart piezoelectric lattices. This application highlights the multifunctional utility of the designed piezoelectric materials. Figure 7d,e shows the optical images of the glove when it hits a wall by a direct strike and right hook, respectively. Spatial distribution of force magnitudes obtained from the prescribed electrodes attached on the lattice is then displayed onto the receiving device, as shown in Figure 7f,g. The red shaded area denotes the probing points while the dashed lines denote other locations where the electrodes can be attached to read data output. Additionally, the impact force distribution restored at grid pattern can be interpolated to cover the entire area. Testing of over 6000 times punching was conducted to confirm the repeatability and durability of these lattice materials (Figure S6b, Supporting Information).

3. Conclusion

In this work, we demonstrated a class of piezoelectric materials with high piezoelectric responsiveness and compliance via exploiting the effects of the nanoparticle-matrix functionalization on the electromechanical performance of the piezoelectric nanocomposite. We proposed a generalized effective interphase model to quantify the electromechanical properties of the 3D printable nanocomposite. We show through theoretical, numerical calculations, and experimental measurements that, increasing the surface functionalization level enables an effective interphase region which enhances the electromechanical performance of the piezoelectric nanocomposite. Maximizing the surface functionalization level approaches the upper bound of piezoelectric coefficient at a given particle loading and enables uniform 3D printable dispersion despite high piezoelectric

particle loading over 30 vol% (≈74 wt%), as compared to the 3 vol% (≈17 wt%). Our design and additive manufacturing routes allow for achieving target flexibilities while keeping high piezoelectric responses via rational designs of inclusion morphologies and monomer stiffness of the constituent materials. Our approach enables printing transducers and smart wearables with arbitrary, complex microscale architectures, and are compatible with commercially available light-based processes. It introduces a new paradigm for smart materials, where wearables, cushions, and structures are themselves responsive and capable of providing 3D stress sensing data without the needs for integrating sensor patches. The designed 3D printable piezo-

Supporting Information

Supporting Information is available from the Wiley Online Library or from the author.

electric nanocomposites that go beyond the existing compliance

and functional property tradeoff highlight their potentials as the

next generation of flexible self-sensing materials and wearables.

Acknowledgements

The authors acknowledge funding from the ICTAS Junior Faculty Award, Office of Naval Research Young Investigator Award NSF CMMI1727492, the Air Force Office of Scientific Research (FA9550-18-1-0299), DARPA Young Faculty Award, and the Office of Naval Research (N00014-18-1-2553) for supporting this work. X.Z. supervised and designed the research. D.Y. performed the calculation of the effective interphase model, numerical calculations, and experimental characterizations via nanoindentation. R.H., H.C. synthesized, and 3D printed the materials and performed experimental studies. X.Z., K.M., F.W., S.B., D.B., G.Y., H.C., P.S., helped with the conceptualization and instrumentation of wireless sensing. All authors contributed to data interpretation, analysis, and drafting of the manuscripts.

Conflict of Interest

An international patent has been filled PCT/US2019/034065. No other competing interests declared.

Keywords

3D printing, flexible, interphase, upper bound, wearable

Received: May 15, 2019 Revised: June 27, 2019 Published online:

a) T. H. Ng, W. H. Liao, J. Intell. Mater. Syst. Struct. 2005, 16, 785;
 b) H. C. Cui, R. Hensleigh, D. S. Yao, D. Maurya, P. Kumar, M. G. Kang, S. Priya, X. Y. Zheng, Nat. Mater. 2019, 18, 234;
 c) X. L. Zhao, H. D. Gao, G. F. Zhang, B. Ayhan, F. Yan, C. Kwan, J. L. Rose, Smart Mater. Struct. 2007, 16, 1208.

 ^[2] a) F. R. Fan, W. Tang, Z. L. Wang, Adv. Mater. 2016, 28, 4283;
 b) G. K. Ottman, H. F. Hofmann, A. C. Bhatt, G. A. Lesieutre, IEEE Trans. Power Electron. 2002, 17, 669;
 c) X. Lu, H. Qu, M. Skorobogatiy, ACS Nano 2017, 11, 2103.



MATERIALS

www.afm-journal.de

- [3] a) M. D. Williams, B. A. Griffin, T. N. Reagan, J. R. Underbrink, M. Sheplak, J. Microelectromech. Syst. 2012, 21, 270; b) M. L. Kuntzman, J. G. Lee, N. N. Hewa-Kasakarage, D. Kim, N. A. Hall, Appl. Phys. Lett. 2013, 102; c) Y. S. Zhang, R. Bauer, J. F. C. Windmill, D. Uttamchandani, Proc. IEEE Micro Electro 2016, 1114.
- [4] a) T. Kanda, A. Makino, T. Ono, K. Suzumori, T. Morita, M. K. Kurosawa, Sens. Actuators, A 2006, 127, 131; b) K. A. Klicker, J. V. Biggers, R. E. Newnham, J. Am. Ceram. Soc. 1981, 64, 5; c) J. H. Nieuwenhuis, J. J. Neumann, D. W. Greve, I. J. Oppenheim, IEEE Trans. Ultrason. Ferr. 2005, 52, 2103.
- [5] Y. Chen, K. Mei, C. M. Wong, D. M. Lin, H. L. W. Chan, J. Y. Dai, Actuators 2015, 4, 127.
- [6] a) H. Kim, F. Torres, D. Villagran, C. Stewart, Y. R. Lin, T. L. B. Tseng, Macromol. Mater. Eng. 2017, 302; b) F. W. Qi, N. Chen, Q. Wang, Mater. Design 2018, 143, 72.
- [7] F. Maillard, E. R. Savinova, U. Stimming, J. Electroanal. Chem. 2007, 599, 221.
- [8] D. W. Sundstrom, Rheol. Acta 1983, 22, 420.
- [9] M. L. Griffith, J. W. Halloran, J. Am. Ceram. Soc. 1996, 79, 2601.
- [10] E. H. Wong, S. W. Koh, K. H. Lee, R. Rajoo, 52nd Electronic Components & Technology Conf. 2002, pp. 1297–1303.
- [11] K. Kim, J. L. Middlebrook, J. E. Chen, W. Zhu, S. C. Chen, D. J. Sirbuly, ACS Appl. Mater. Interfaces 2016, 8, 33394.
- [12] K. Kim, W. Zhu, X. Qu, C. Aaronson, W. R. McCall, S. C. Chen, D. J. Sirbuly, ACS Nano 2014, 8, 9799.
- [13] A. Kumar, D. Chakraborty, Mater. Design 2009, 30, 1216.
- [14] R. A. Sperling, W. J. Parak, Philos. Trans. R. Soc., A 2010, 368, 1333.
- [15] M. Jabbari, J. Hattel, Mater. Sci. Technol. 2014, 30, 283.
- [16] H. Kim, F. Torres, Y. Y. Wu, D. Villagran, Y. R. Lin, T. L. Tseng, Smart Mater. Struct. 2017, 26.
- [17] Y. Mikata, Int. J. Solids Struct. 2001, 38, 7045.
- [18] B. T. Wang, C. A. Rogers, J. Compos. Mater. 1991, 25, 433.

- [19] M. Taya, Electronic Composites, Cambridge University Press, Cambridge 2009.
- [20] a) National Aeronautics and Space Administration, Theory of Fiber Reinforced Materials, NASA, Washington, DC 1972;
 b) A. Nafari, H. A. Sodano, Nano Energy 2019, 60, 620;
 c) A. Nafari, H. A. Sodano, Voltage coefficient of a piezoelectric nanocomposite energy harvester: modeling and experimental verification, SPIE, Bellingham, Washington USA 2019;
 d) S. Iyer, T. A. Venkatesh, Int. J. Solids Struct. 2014, 51, 1221;
 e) C. H. Lin, A. Muliana, J. Intell. Mater. Syst. Struct. 2014, 25, 1306.
- [21] S. T. Knauert, J. F. Douglas, F. W. Starr, J. Polym. Sci., Polym. Phys. 2007, 45, 1882.
- [22] Y. Benveniste, Mech. Mater. 1987, 6, 147.
- [23] M. G. Todd, F. G. Shi, J. Appl. Phys. 2003, 94, 4551.
- [24] A. C. Fischer-Cripps, Nanoindentation, Mechanical Engineering Series, New York, NY 2011, p. 21.
- [25] A. Hodzic, Z. H. Stachurski, J. K. Kim, Polymer 2000, 41, 6895.
- [26] COMSOL Multiphysics v. 5.3, COMSOL AB, Stockholm, Sweden, www.comsol.com.
- [27] a) R. Kar-Gupta, T. A. Venkatesh, Acta Mater. 2008, 56, 3810;
 b) D. Chen, X. Y. Zheng, Sci-Rep UK 2018, 8, 9139;
 c) N. J. R. K. Gerard,
 H. C. Cui, C. Shen, Y. B. Xie, S. Cummer, X. Y. Zheng, Y. Jing, Appl. Phys. Lett. 2019, 114, 231902.
- [28] J. El Ouafi, L. Azrar, A. A. Aljinaidi, J. Intell. Mater. Syst. Struct. 2016, 27, 1600.
- [29] a) D. Grinberg, S. Siddique, M.-Q. Le, R. Liang, J.-F. Capsal, P.-J. Cottinet, J. Polym. Sci., Part B: Polym. Phys. 2019, 57, 109;
 b) B. Tiller, A. Reid, B. T. Zhu, J. Guerreiro, R. Domingo-Roca, J. C. Jackson, J. F. C. Windmill, Mater. Design 2019, 165; c) J. I. Park, G. Y. Lee, J. Yang, C. S. Kim, S. H. Ahn, J. Compos. Mater. 2016, 50, 1573; d) X. F. Chen, H. O. T. Ware, E. Baker, W. S. Chu, J. M. Hu, C. Sun, Proc. CIRP 2017, 65, 157.